

Article

Localization and delocalization of light in photonic moiré lattices

<https://doi.org/10.1038/s41586-019-1851-6>

Received: 9 January 2019

Accepted: 12 September 2019

Published online: 18 December 2019

Peng Wang^{1,2,8}, Yuanlin Zheng^{1,2,8}, Xianfeng Chen^{1,2}, Changming Huang³, Yaroslav V. Kartashov^{4,5}, Lluís Torner^{4,6}, Vladimir V. Konotop⁷ & Fangwei Ye^{1,2*}

Moiré lattices consist of two superimposed identical periodic structures with a relative rotation angle. Moiré lattices have several applications in everyday life, including artistic design, the textile industry, architecture, image processing, metrology and interferometry. For scientific studies, they have been produced using coupled graphene–hexagonal boron nitride monolayers^{1,2}, graphene–graphene layers^{3,4} and graphene quasicrystals on a silicon carbide surface⁵. The recent surge of interest in moiré lattices arises from the possibility of exploring many salient physical phenomena in such systems; examples include commensurable–incommensurable transitions and topological defects², the emergence of insulating states owing to band flattening^{3,6}, unconventional superconductivity⁴ controlled by the rotation angle^{7,8}, the quantum Hall effect⁹, the realization of non-Abelian gauge potentials¹⁰ and the appearance of quasicrystals at special rotation angles¹¹. A fundamental question that remains unexplored concerns the evolution of waves in the potentials defined by moiré lattices. Here we experimentally create two-dimensional photonic moiré lattices, which—unlike their material counterparts—have readily controllable parameters and symmetry, allowing us to explore transitions between structures with fundamentally different geometries (periodic, general aperiodic and quasicrystal). We observe localization of light in deterministic linear lattices that is based on flat-band physics⁶, in contrast to previous schemes based on light diffusion in optical quasicrystals¹², where disorder is required¹³ for the onset of Anderson localization¹⁴ (that is, wave localization in random media). Using commensurable and incommensurable moiré patterns, we experimentally demonstrate the two-dimensional localization–delocalization transition of light. Moiré lattices may feature an almost arbitrary geometry that is consistent with the crystallographic symmetry groups of the sublattices, and therefore afford a powerful tool for controlling the properties of light patterns and exploring the physics of periodic–aperiodic phase transitions and two-dimensional wavepacket phenomena relevant to several areas of science, including optics, acoustics, condensed matter and atomic physics.

One of the most salient properties of an engineered optical system is its capability to affect a light beam in a prescribed manner, such as to control its diffraction pattern or to localize it. The importance of wavepacket localization extends far beyond optics and impacts all branches of science dealing with wave phenomena. Homogeneous or strictly periodic linear systems cannot result in wave localization, and the latter require the presence of structure defects or nonlinearity. Anderson localization¹⁵ is a hallmark discovery in condensed-matter physics. All electronic states in one- and two-dimensional potentials with uncorrelated disorder are localized. Three-dimensional systems with disordered potentials are known to have both localized and

delocalized eigenstates¹⁴, separated by an energy known as the mobility edge¹⁶. Coexistence of localized and delocalized eigenstates has been predicted also in regular quasiperiodic one-dimensional systems, first in the discrete Aubry–André¹⁷ model and later in continuous optical and matter-wave systems^{18–20}. Quasiperiodic (or aperiodic) structures, even those that possess long-range order, fundamentally differ both from periodic systems, where all eigenmodes are delocalized Bloch waves, and from disordered media, where all states are localized (in one or two dimensions). Upon variation of the parameters of a quasiperiodic system, it is possible to observe the transition between localized and delocalized states. Such a localization–delocalization transition (LDT)

¹School of Physics and Astronomy, Shanghai Jiao Tong University, Shanghai, China. ²State Key Laboratory of Advanced Optical Communication Systems and Networks, Shanghai Jiao Tong University, Shanghai, China. ³Department of Electronic Information and Physics, Changzhi University, Shanxi, China. ⁴ICFO-Institut de Ciències Fotoniques, The Barcelona Institute of Science and Technology, Castelldefels, Spain. ⁵Institute of Spectroscopy, Russian Academy of Sciences, Troitsk, Russia. ⁶Universitat Politècnica de Catalunya, Barcelona, Spain. ⁷Departamento de Física y Centro de Física Teórica e Computacional, Faculdade de Ciências, Universidade de Lisboa, Lisbon, Portugal. ⁸These authors contributed equally: Peng Wang, Yuanlin Zheng. *e-mail: fangweiye@sjtu.edu.cn

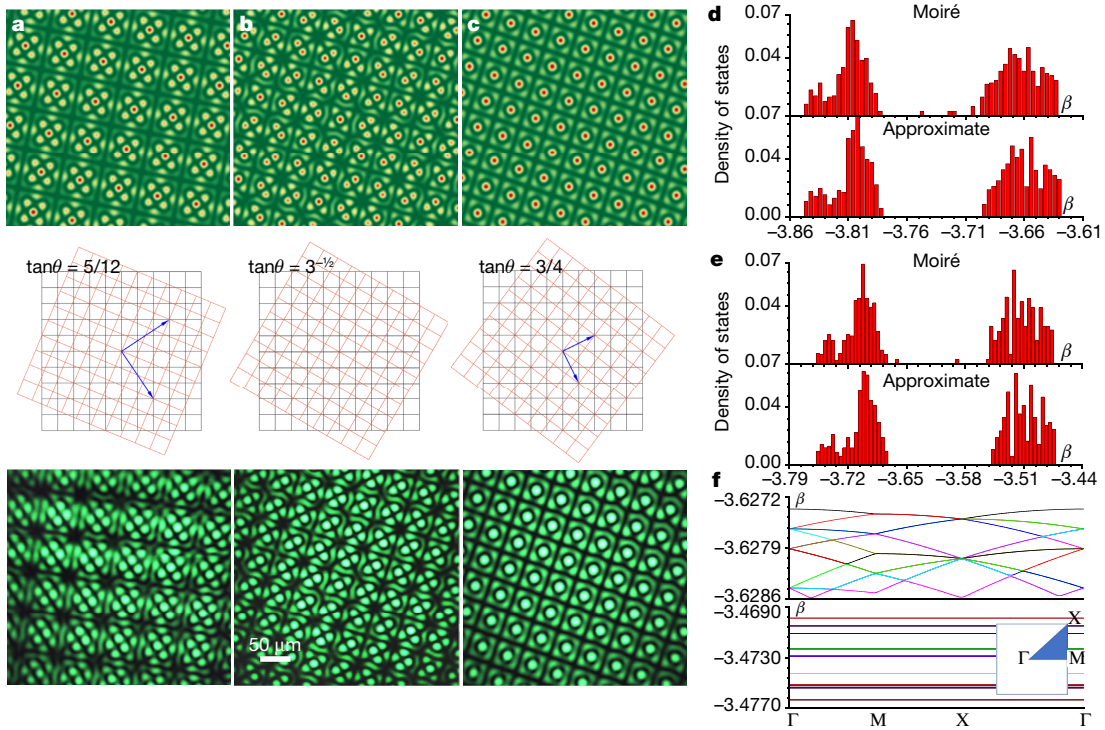


Fig. 1 | Moiré lattices, density of states and band structures. **a–c**, Moiré lattices with lattice intensity $I(\mathbf{r})$, generated by two interfering square sublattices with $p_1 = p_2$ and axes mutually rotated by the angle indicated in each panel. Top row, calculated patterns. Middle row, schematic discrete representation of two rotated sublattices. Bottom row, experimental patterns at the output face of the crystal. The scale is the same for all images.

d, e, Comparison of the density of states calculated for a moiré lattice (top) and its periodic approximation (bottom) at $p_2 = 0.1$ (**d**) and $p_2 = 0.2$ (**e**). The approximate Pythagorean lattice has period $b_1 = \sqrt{3361}\pi$ (see Supplementary Information). **f**, Band structures for a periodic lattice approximating a moiré lattice at $p_2 = 0.1$ (top; 15 upper bands are shown) and $p_2 = 0.2$ (bottom; 68 upper bands are shown). In all cases $p_1 = 1$.

has been observed in one-dimensional quasiperiodic optical²¹ and in atomic systems^{22,23}.

Wave localization is sensitive to the dimensionality of the physical setting. Anderson localization and a mobility edge in two-dimensional systems were first reported in experiments with bending waves²⁴ and later in optically induced disordered lattices²⁵. In quasicrystals, localization has been observed only under the action of nonlinearity¹² and in the presence of strong disorder¹³. Although localization and delocalization of light in two-dimensional systems without any type of disorder and nonlinearity have been predicted theoretically for moiré lattices²⁶ and very recently for Vogel spirals²⁷, the phenomenon has never been observed experimentally.

Here we report the first, to our knowledge, experimental realization of reconfigurable photonic moiré lattices with controllable parameters and symmetry. The lattices are induced by two superimposed periodic patterns²⁸ (sublattices) with either square or hexagonal primitive cells, and have tunable amplitudes and twist angle. Depending on the twist angle, a photonic moiré lattice may have different periodic (commensurable) structure or aperiodic (incommensurable) structure without translational periodicity, but it always features the rotational symmetry of the sublattices. Moiré lattices can also transform into quasicrystals with higher rotational symmetry¹¹. The angles at which a commensurable phase (periodicity) of a moiré lattice is achieved are determined by Pythagorean triples in the case of square sublattices²⁶, or by another Diophantine equation when the primitive cell of the sublattices is not a square (see Methods). For all other rotation angles, the structure is aperiodic albeit regular (that is, it is not disordered). Changing the relative amplitudes of the sublattices allows us to smoothly tune the shape of the lattice without affecting its rotational symmetry.

In contrast to crystalline moiré lattices^{1–5}, optical patterns are monolayer structures; that is, both sublattices interfere in one plane. As a

consequence, light propagating in such media is described by a one-component field. In the paraxial approximation, the propagation of an extraordinarily polarized beam in a photorefractive medium with an optically induced refractive index is governed by the Schrödinger equation for the dimensionless field amplitude²⁹ $\psi(\mathbf{r}, z)$:

$$i \frac{\partial \psi}{\partial z} = -\frac{1}{2} \nabla^2 \psi + \frac{E_0}{1+I(\mathbf{r})} \psi \quad (1)$$

Here $\nabla = (\partial/\partial x, \partial/\partial y)$; $\mathbf{r} = (x, y)$ is the radius vector in the transverse plane, scaled to the wavelength $\lambda = 632.8$ nm of the beam used in the experiments; z is the propagation distance, scaled to the diffraction length $2\pi n_e \lambda$; n_e is the refractive index of the homogeneous crystal for extraordinarily polarized light; $E_0 > 0$ is the dimensionless applied d.c. field; $I(\mathbf{r}) = |p_1 V(\mathbf{r}) + p_2 V(S\mathbf{r})|^2$ is the intensity of the moiré lattice induced by two ordinarily polarized mutually coherent periodic sublattices, $V(\mathbf{r})$ and $V(S\mathbf{r})$, interfering in the (x, y) plane and rotated by angle θ with respect to each other (see Methods); $S = S(\theta)$ is the operator of the two-dimensional rotation; and p_1 and p_2 are the amplitudes of the first and second sublattices, respectively. The number of laser beams creating each sublattice $V(\mathbf{r})$ depends on the desired lattice geometry. The form in which the lattice intensity $I(\mathbf{r})$ enters equation (1) is determined by the mechanism of the photorefractive response.

To visualize the formation of moiré lattices, it is convenient to associate a continuous sublattice $V(\mathbf{r})$ with a discrete one that has lattice vectors determined by the locations of the absolute maxima of $V(\mathbf{r})$. The resulting moiré pattern inherits the rotational symmetry of $V(\mathbf{r})$. At specific angles some nodes of different sublattices may coincide, thereby leading to translational symmetry of the moiré pattern in the commensurable phase; see the primitive translation vectors illustrated by blue arrows in Fig. 1a, c for the case of square sublattices. The rotation

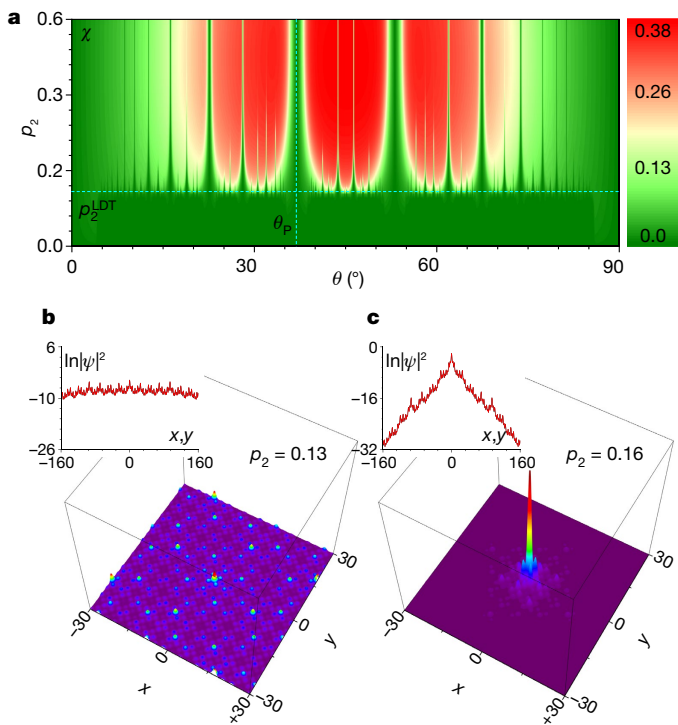


Fig. 2 | Form factor and moiré states. **a**, Form factor (inverse width) of the eigenmodes with largest β versus rotation angle θ and versus the amplitude of the second sublattice, p_2 , at $p_1=1$. The horizontal dashed line indicates the sublattice depth p_2^{LDT} at which LDT occurs. The vertical dashed line shows one of the Pythagorean angles $\theta_0 = \arctan(3/4)$. **b, c**, Examples of mode profiles with the largest β for $p_2 < p_2^{\text{LDT}}$ (**b**) and $p_2 > p_2^{\text{LDT}}$ (**c**). The insets show cuts of the $\ln|\psi|^2$ distribution along the x and y axes.

angles at which the periodicity of $I(\mathbf{r})$ is achieved are determined by triples of positive integers $(a, b, c) \in \mathbb{N}$ related by a Diophantine equation characteristic for a given sublattice²⁶ (see Extended Data Table 1).

First, we consider a Pythagorean lattice created by two square sublattices. For rotation angles θ such that $\cos\theta = a/c$ and $\sin\theta = b/c$, where (a, b, c) is a Pythagorean triple (that is, $a^2 + b^2 = c^2$), $I(\mathbf{r})$ is a periodic moiré lattice. Such angles are hitherto referred to as Pythagorean. For all other, non-Pythagorean, rotation angles θ , the lattice $I(\mathbf{r})$ is aperiodic. Figure 1a–c compares calculated $I(\mathbf{r})$ patterns (first row) with lattices created experimentally²⁹ in a biased SBN:61 photorefractive crystal with dimensions $5 \times 5 \times 20 \text{ mm}^3$ (third row) for different rotation angles. The second row shows the respective discrete moiré lattices. Figure 1a, c shows periodic lattices, whereas Fig. 1b gives an example of an aperiodic lattice. All results were obtained for $E_0 = 7$, which corresponds to a d.c. electric field of $8 \times 10^4 \text{ V m}^{-1}$ applied to the crystal. The amplitude of the first sublattice was set to $p_1 = 1$ in all cases, which corresponds to an average intensity of $I_{av} \approx 3.8 \text{ mW cm}^{-2}$. For such parameters, the refractive index modulation depth in the moiré lattice is of the order of $\delta n \approx 10^{-4}$.

Mathematically, incommensurable lattices are almost periodic functions³⁰. Any non-Pythagorean twist angle can be approached by a Pythagorean one with any prescribed accuracy (see Supplementary Information). Thus, any finite area of an incommensurable moiré lattice can be approached by a primitive effective cell of some periodic Pythagorean lattice, whereas a more accurate approximation requires a larger primitive cell of the Pythagorean lattice. This property is illustrated in Fig. 1d, e by the quantitative similarities between the densities of states calculated for an incommensurable lattice and its effective-cell approximation. A remarkable property of Pythagorean lattices is the extreme flattening of the higher bands that occurs when the ratio p_2/p_1 exceeds a certain threshold (Fig. 1f). The number of flat bands grows with the size of the area of the primitive cell of the Pythagorean lattice

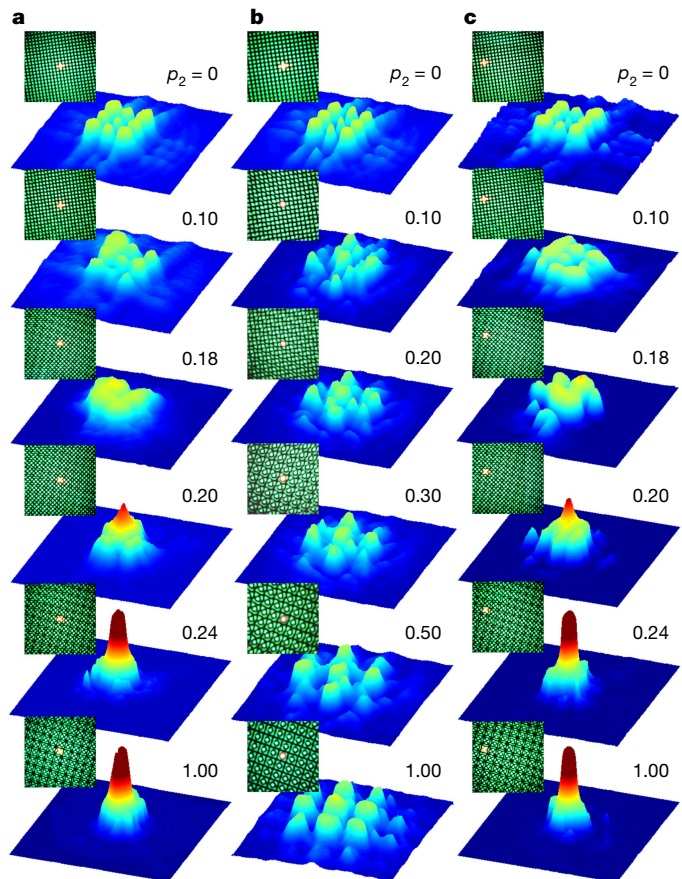


Fig. 3 | Output patterns of light propagating through moiré lattices. **a–c**, Observed output intensity distributions, illustrating LDT with increasing amplitude p_2 of the second sublattice for rotation angle $\theta = \arctan 3^{-1/2} = \pi/6$ (**a**, **c**) and absence of LDT for the Pythagorean angle $\theta = \arctan(3/4)$ (**b**). The insets show the location of the excitation: central (**a, b**) and off-centre (**c**).

approximation. Thus, an incommensurable moiré lattice can be viewed as the large-area limit of a periodic Pythagorean lattice with extremely flat higher bands. We note that the existence of flat bands for twisted bilayer graphene was discussed in refs.^{7,8,31}. Because flat bands support quasi-nondiffracting localized modes, an initially localized beam launched into such a moiré lattice will remain localized. This flat-band physics of moiré lattices, which is fundamentally different from that of Anderson localization in random media, allows us to predict light localization above a threshold value of the ratio p_2/p_1 . Furthermore, flat bands support states that are exponentially localized in the primitive cell and that can be well approximated by exponentially localized two-dimensional Wannier functions³² (see Fig. 2c and Supplementary Information).

To elucidate the impact of the sublattice amplitudes and rotation angle θ on the light localization, we calculated the linear eigenmodes $\psi(\mathbf{r}, z) = w(\mathbf{r})e^{i\beta z}$ (where β is the propagation constant and $w(\mathbf{r})$ is the mode profile) supported by the moiré lattices. To characterize their localization we use the integral form factor $\chi = (U^{-2} \iint |\psi|^4 d^2\mathbf{r})^{1/2}$, where $U = \iint |\psi|^2 d^2\mathbf{r}$ is the energy flow (the integration is over the transverse area of the crystal). The form factor is inversely proportional to the mode width: the larger the value of χ , the stronger the localization. The dependence of the form factor of the most localized mode (the mode with largest β) on θ and p_2 is shown in Fig. 2a (for modes with lower values of β , the dependencies are qualitatively similar). One observes a sharp LDT above a certain threshold depth p_2^{LDT} of the second sublattice, at the amplitude of the first sublattice, $p_1=1$. Below p_2^{LDT} all modes are extended (Fig. 2b), and above the threshold some modes are

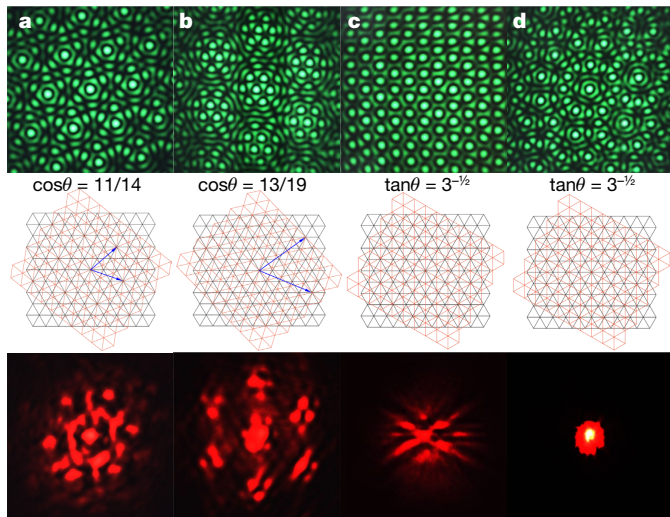


Fig. 4 | Moiré lattices created by superposition of two rotated hexagonal lattices. **a–d**, Top row, moiré lattices produced by the interference of two hexagonal patterns rotated by angle θ with $p_2=1$ (**a**, **b**, **d**) and $p_2=0.18$ (**c**). Middle row, schematic discrete representation of two rotated hexagonal sublattices. Bottom row, measured output-intensity distributions for the signal beam at the output face of the crystal. In all cases $p_1=1$. Blue arrows in the middle panels of **a** and **b** indicate the primitive translation vectors of the corresponding discrete lattice.

localized (Fig. 2c). This is consistent with the extreme band flattening of the approximate Pythagorean lattice at $p_2 > p_2^{\text{LDT}}$ (Fig. 1f). The inset in Fig. 2c reveals exponential tails for $p_2 > p_2^{\text{LDT}}$, from which the localization length for the most localized mode can be extracted.

Figure 2a shows delocalization for angles θ set by the Pythagorean triples when all modes are extended, regardless of the value of p_2 . It also reveals that p_2^{LDT} is practically independent of the non-Pythagorean rotation angle. This is explained by the fact that a large fraction of the power in a localized mode resides in the vicinity of a lattice maximum (that is, at $\mathbf{r}=0$). In an incommensurable phase, when $I(\mathbf{r}) < I(0)$, for all $\mathbf{r} \neq 0$ the optical potential can be approximated by the Taylor expansion of $E_0/[1+I(\mathbf{r})]$ with respect to \mathbf{r} near the origin. Such expansion includes the rotation angle θ only in the fourth order (see Supplementary Information) and therefore locally can be viewed as almost isotropic.

To study the guiding properties of the Pythagorean moiré lattices experimentally, we measured the diffraction outputs for beams propagating in lattices corresponding to different rotation angles θ for a fixed input position of the beam, centred or off-centre. The diameter of the Gaussian beam focused on the input face of the crystal was about $23\text{ }\mu\text{m}$, covering approximately one bright spot (channel) of the lattice profile. The intensity of the input beam was about 10 times lower than the intensity of the lattice-creating beam, I_{av} , to guarantee that the beam did not distort the induced refractive index and that it propagated in the linear regime.

Experimental evidence of LDT in the two-dimensional lattice is presented in Fig. 3, where we compare output patterns for the low-power light beam in the incommensurable ($\tan\theta=3^{-1/2}$; Fig. 3a and Fig. 3c for central and off-centre excitations, respectively) and commensurable ($\tan\theta=3/4$, Fig. 3b) moiré lattices, tuning in parallel the amplitude p_2 of the second sublattice. When $p_2 < p_2^{\text{LDT}}$ (in Fig. 3 $p_2^{\text{LDT}} \approx 0.15$), the light beam in the incommensurable lattice notably diffracts upon propagation and expands across multiple local maxima of $I(\mathbf{r})$ in the vicinity of the excitation point. However, when p_2 exceeds the LDT threshold, it is readily visible that diffraction is arrested for both central (Fig. 3a) and off-centre (Fig. 3c) excitations and a localized spot is observed at the output over a large range of p_2 values. In clear contrast, localization is absent for any p_2 value in the periodic lattice associated with the

Pythagorean triple (Fig. 3b). Additional proof of the LDT is reported in Extended Data Fig. 1. We compare experimental and theoretical results for propagation at $p_1=1$. In an incommensurable lattice, at $p_2 < p_2^{\text{LDT}}$ one observes beam broadening (top row). Localization takes place at $p_2 > p_2^{\text{LDT}}$ (middle row). At a Pythagorean twist angle, localization does not occur even for $p_2=p_1=1$ (bottom row). Simulations of the propagation to much larger distances beyond the available sample length (Extended Data Fig. 2) confirm localization of the beam in the incommensurable lattice at any distance at $p_2 > p_2^{\text{LDT}}$ and its expansion at $p_2 < p_2^{\text{LDT}}$.

The mutual rotation of two identical sublattices allows the generation of commensurable and incommensurable moiré patterns with sublattices of any allowed symmetry. To illustrate the universality of LDT, we created hexagonal moiré lattices using an induction technique similar to that used for single honeycomb photonic lattices³³. For such lattices, the rotation angles producing commensurable patterns are given by the relation $\tan\theta=b\sqrt{3}/(2a+b)$, where the integers a , b and c solve the Diophantine equation $a^2+b^2+ab=c^2$. Two examples are presented in Fig. 4a, b. In such periodic structures, the light beam experiences considerable diffraction for any amplitude of the sublattices, as shown in the bottom row. To observe LDT, one has to induce aperiodic structures. To this end, we set the rotation angle to 30° . In this incommensurable case, we did observe LDT by increasing the amplitude of the second sublattice, keeping the amplitude p_1 fixed. Delocalized and localized output beams are shown in the lower panels of Fig. 4c, d. In Fig. 4c the ideal six-fold rotation symmetry of the output pattern is slightly distorted, presumably owing to the intrinsic anisotropy of the photorefractive response. At $p_2=p_1$ the moiré pattern acquires a 12-fold rotational symmetry (shown in Fig. 4d), as proposed in ref.¹¹ as a model of a quasicrystal, and similar to the twisted bilayer graphene quasicrystal reported in ref.⁵.

Moiré lattices can be created in practically any arbitrary configuration consistent with two-dimensional symmetry groups, thus allowing the creation of potentials that may not be easily produced in tunable form using material structures. In addition to their direct application to the control of light patterns, the availability of photonic moiré patterns allows the study of phenomena relevant to other areas of physics, particularly to condensed matter, which are harder to explore directly. An outstanding example is the relation between conductivity/transport and the symmetry of incommensurable patterns with long-range order. The concept can be also extended to atomic physics and in particular to Bose–Einstein condensates, where potentials are created using similar geometries (and where Anderson localization has been observed³⁴). Finally, we note that whereas most previous studies of moiré lattices were focused on graphene and quasicrystals, our results suggest that the photonic counterpart affords a powerful platform for the creation of synthetic settings to investigate wavepacket localization and flat-band phenomena in two-dimensional systems at large.

Online content

Any methods, additional references, Nature Research reporting summaries, source data, extended data, supplementary information, acknowledgements, peer review information; details of author contributions and competing interests; and statements of data and code availability are available at <https://doi.org/10.1038/s41586-019-1851-6>.

1. Decker, R. et al. Local electronic properties of graphene on a BN substrate via scanning tunnelling microscopy. *Nano Lett.* **11**, 2291–2295 (2011).
2. Woods, C. R. et al. Commensurate–incommensurate transition in graphene on hexagonal boron nitride. *Nat. Phys.* **10**, 451–456 (2014).
3. Cao, Y. et al. Correlated insulator behaviour at half-filling in magic-angle graphene superlattices. *Nature* **556**, 80–84 (2018).
4. Cao, Y. et al. Unconventional superconductivity in magic-angle graphene superlattices. *Nature* **556**, 43 (2018).
5. Ahn, S. J. et al. Dirac electrons in a dodecagonal graphene quasicrystal. *Science* **361**, 782–786 (2018).

6. MacDonald, A. H. Bilayer graphene's wicked, twisted road. *Physics* **12**, 12 (2019).
7. Bistritzer, R. & MacDonald, A. H. Moiré bands in twisted double-layer graphene. *Proc. Natl. Acad. Sci. USA* **108**, 12233–12237 (2011).
8. Tarnopolsky, G., Kruchkov, A. J. & Vishwanath, A. Origin of magic angles in twisted bilayer graphene. *Phys. Rev. Lett.* **122**, 106405 (2019).
9. Dean, C. R. et al. Hofstadter's butterfly and the fractal quantum Hall effect in moiré superlattices. *Nature* **497**, 598–602 (2013).
10. San-Jose, P., González, J. & Guinea, F. Non-Abelian gauge potentials in graphene bilayers. *Phys. Rev. Lett.* **108**, 216802 (2012).
11. Stampfli, P. A dodecagonal quasiperiodic lattice in two dimensions. *Helv. Phys. Acta* **59**, 1260–1263 (1986).
12. Freedman, B. et al. Wave and defect dynamics in nonlinear photonic quasicrystals. *Nature* **440**, 1166–1169 (2006).
13. Levi, L. et al. Disorder-enhanced transport in photonic quasicrystals. *Science* **332**, 1541 (2011).
14. Abrahams, E., Anderson, P. W., Licciardello, D. C. & Ramakrishnan, T. V. Scaling theory of localization: absence of quantum diffusion in two dimensions. *Phys. Rev. Lett.* **42**, 673–676 (1979).
15. Brandes, T. & Kettemann, S. *The Anderson Transition and its Ramifications: Localization, Quantum Interference, and Interactions* (Springer, 2003).
16. Mott, N. The mobility edge since 1967. *J. Phys. C* **20**, 3075–3102 (1987).
17. Aubry, S. & André, G. Analyticity breaking and Anderson localization in incommensurate lattices. *Ann. Isr. Phys. Soc.* **3**, 133 (1980).
18. Boers, D. J., Goedeke, B., Hinrichs, D. & Holthaus, M. Mobility edges in bichromatic optical lattices. *Phys. Rev. A* **75**, 063404 (2007).
19. Modugno, M. Exponential localization in one-dimensional quasi-periodic optical lattices. *New J. Phys.* **11**, 033023 (2009).
20. Li, C., Ye, F., Kartashov, Y. V., Konotop, V. V. & Chen, X. Localization–delocalization transition in spin-orbit-coupled Bose–Einstein condensate. *Sci. Rep.* **6**, 31700 (2016).
21. Lahini, Y. et al. Observation of a localization transition in quasiperiodic photonic lattices. *Phys. Rev. Lett.* **103**, 013901 (2009).
22. Roati, G. et al. Anderson localization of a non-interacting Bose–Einstein condensate. *Nature* **453**, 895–898 (2008).
23. Lüschen, H. P. et al. Single-particle mobility edge in a one-dimensional quasiperiodic optical lattice. *Phys. Rev. Lett.* **120**, 160404 (2018).
24. Ye, L., Cody, G., Zhou, M., Sheng, P. & Norris, A. N. Observation of bending wave localization and quasi mobility edge in two dimensions. *Phys. Rev. Lett.* **69**, 3080–3083 (1992).
25. Schwartz, T., Bartal, G., Fishman, S. & Segev, M. Transport and Anderson localization in disordered two-dimensional photonic lattices. *Nature* **446**, 52–55 (2007).
26. Huang, C. et al. Localization delocalization wavepacket transition in Pythagorean aperiodic potentials. *Sci. Rep.* **6**, 32546 (2016).
27. Sgrignuoli, F., Wang, R., Pinheiro, F. & Dal Negro, L. Localization of scattering resonances in aperiodic Vogel spirals. *Phys. Rev. B* **99**, 104202 (2019).
28. Fleischner, J., Segev, M., Efremidis, N. & Christodoulides, D. Observation of two-dimensional discrete solitons in optically induced nonlinear photonic lattices. *Nature* **422**, 147–150 (2003).
29. Efremidis, N. K., Sears, S., Christodoulides, D. N., Fleischner, J. W. & Segev, M. Discrete solitons in photorefractive optically induced photonic lattices. *Phys. Rev. E* **66**, 046602 (2002).
30. Franklin, P. The elementary theory of almost periodic functions of two variables. *J. Math. Phys.* **5**, 40–54 (1926).
31. Suárez Morell, E., Correa, J. D., Vargas, P., Pacheco, M. & Barticevic, Z. Flat bands in slightly twisted bilayer graphene: tight-binding calculations. *Phys. Rev. B* **82**, 121407 (2010).
32. Brouder, C., Panati, G., Calandra, M., Mourougane, C. & Marzar, N. Exponential localization of Wannier functions in insulators. *Phys. Rev. Lett.* **98**, 046402 (2007).
33. Peleg, O. et al. Conical diffraction and gap solitons in honeycomb photonic lattices. *Phys. Rev. Lett.* **98**, 103901 (2007).
34. Billy, J., Sanchez-Palencia, L., Bouyer, P. & Aspect, A. Direct observation of Anderson localization of matter waves in a controlled disorder. *Nature* **453**, 891–894 (2008).

Publisher's note Springer Nature remains neutral with regard to jurisdictional claims in published maps and institutional affiliations.

© The Author(s), under exclusive licence to Springer Nature Limited 2019

Methods

Experimental setup

The experimental setup is illustrated in Extended Data Fig. 3. The lattice is created using optical induction, as described in ref.²⁹ and was first realized experimentally in ref.²⁸. A continuous-wave frequency-doubled Nd:YAG laser at a wavelength of $\lambda = 532$ nm is divided by a polarizing beam splitter into two polarization components, which are sent to path a and path b separately. Light in path a is extraordinarily polarized and it is used to image the induced potential in the photorefractive crystal (bottom row of Fig. 1). Light in path b is ordinarily polarized and it is used to write the desirable potential landscape in a photorefractive SBN:61 crystal with dimensions $5 \times 5 \times 20$ mm³ and extraordinary refractive index $n_e = 2.2817$. Before entering the crystal, the ordinarily polarized light beam in path b is modulated by masks 1 and 2 and is transformed into a superposition of two rotated periodic patterns. Their relative strength p_2/p_1 —more precisely, the strength of the second lattice—as well as the twist angle θ are controlled by the polarizer-based mask 1 and the amplitude mask 2. A He–Ne laser with wavelength $\lambda = 633$ nm shown in path c provides an extraordinarily polarized beam focused onto the front facet of the crystal, which serves as a probe beam for studying light propagation in the induced potential. We record the output light intensity pattern using a charge-coupled device (CCD) at the exit facet of the crystal after a propagation distance of 20 mm.

Characteristics of moiré lattices used in experiment

Two types of moiré lattices were used in the experiments, and their characteristics are summarized in Extended Data Table 1. In all cases

the centre of rotation in the (x, y) plane was chosen to be coincident with a node of one of the sublattices.

Data availability

The data that support the findings of this study are available from the corresponding author upon reasonable request.

Code availability

The codes that support the findings of this study are available from the corresponding author upon reasonable request.

Acknowledgements P.W. and F.Y. acknowledge support from the NSFC (grant numbers 91950120, 11690033 and 61475101). Y.V.K. and L.T. acknowledge support from the Severo Ochoa Excellence Programme (SEV-2015-0522), Fundació Privada Cellex, Fundació Privada Mir-Puig and CERCA/Generalitat de Catalunya. F.Y. thanks Z. Chen, Y. Hu and D. Song for technical discussions on the experiment with the SBN crystals.

Author contributions All authors contributed significantly to the study.

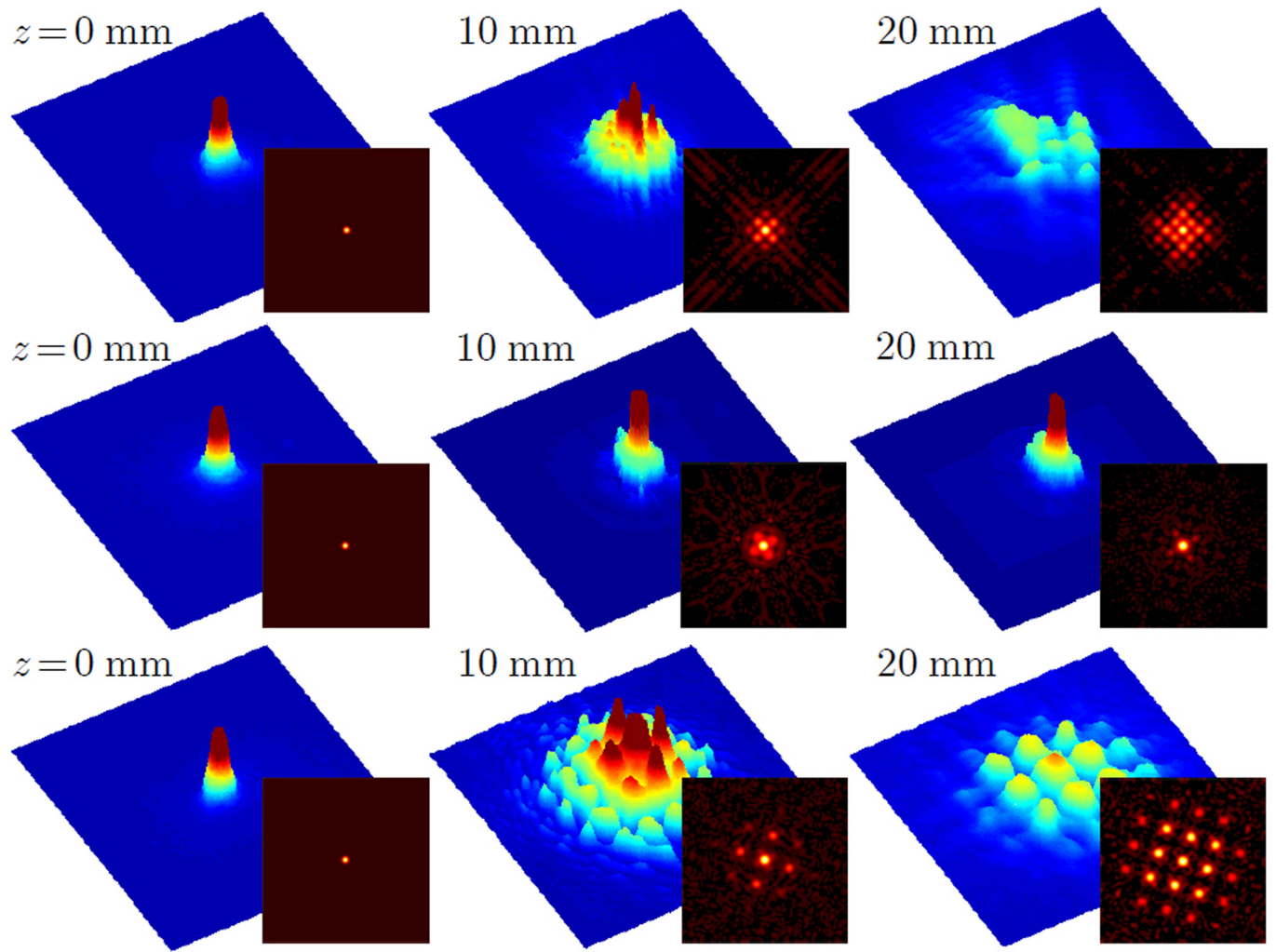
Competing interests The authors declare no competing interests.

Additional information

Supplementary information is available for this paper at <https://doi.org/10.1038/s41586-019-1851-6>.

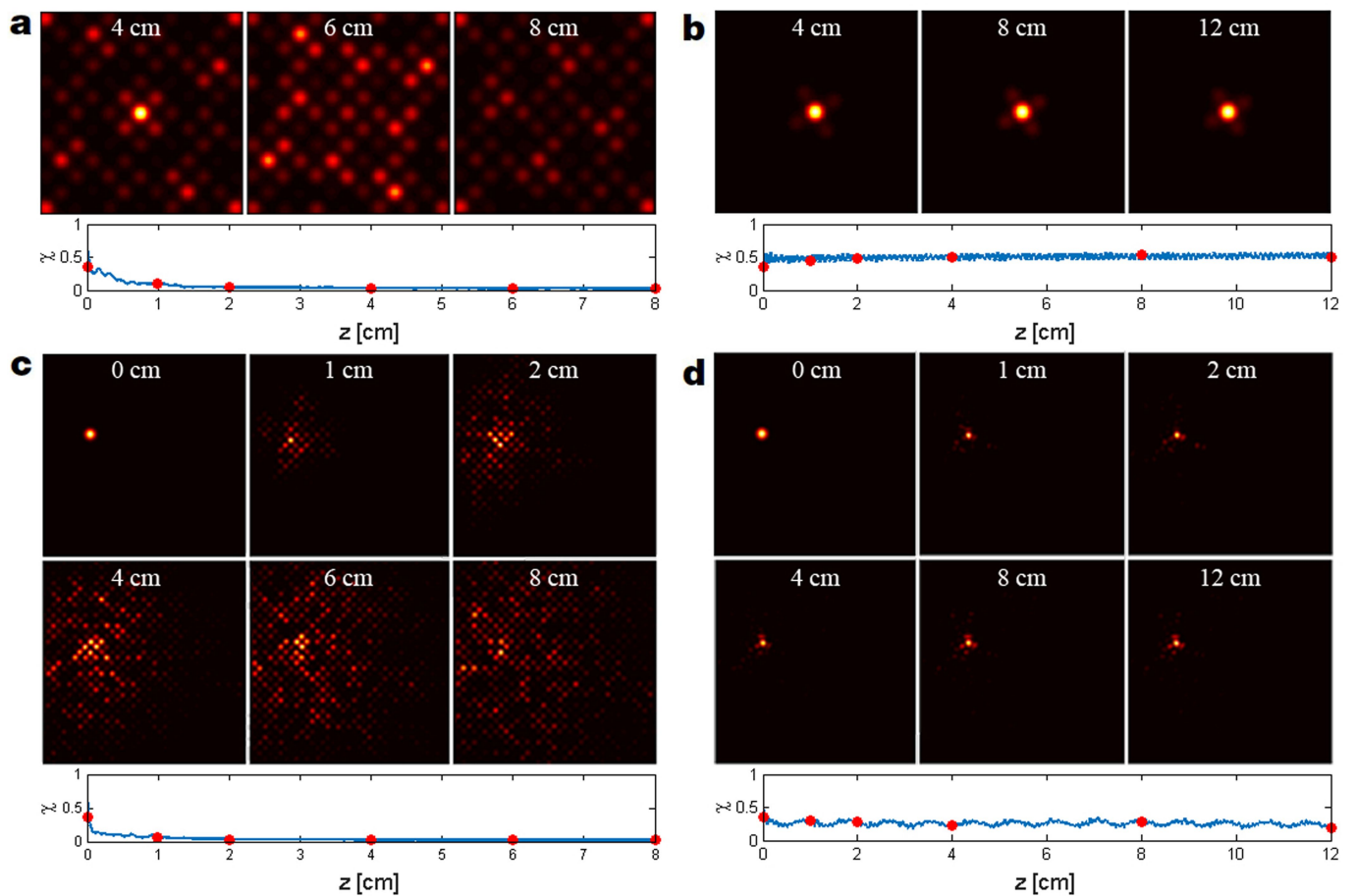
Correspondence and requests for materials should be addressed to F.Y.

Reprints and permissions information is available at <http://www.nature.com/reprints>.



Extended Data Fig. 1 | Evolution of light in moiré lattices. Experimentally observed intensity distributions of the probe beam (colour-surface plots) and corresponding theoretically calculated distributions (insets) at different propagation distances z , for $\tan\theta = 3^{-1/2}$ and $p_2 = 0.1$ (below the LDT point; top

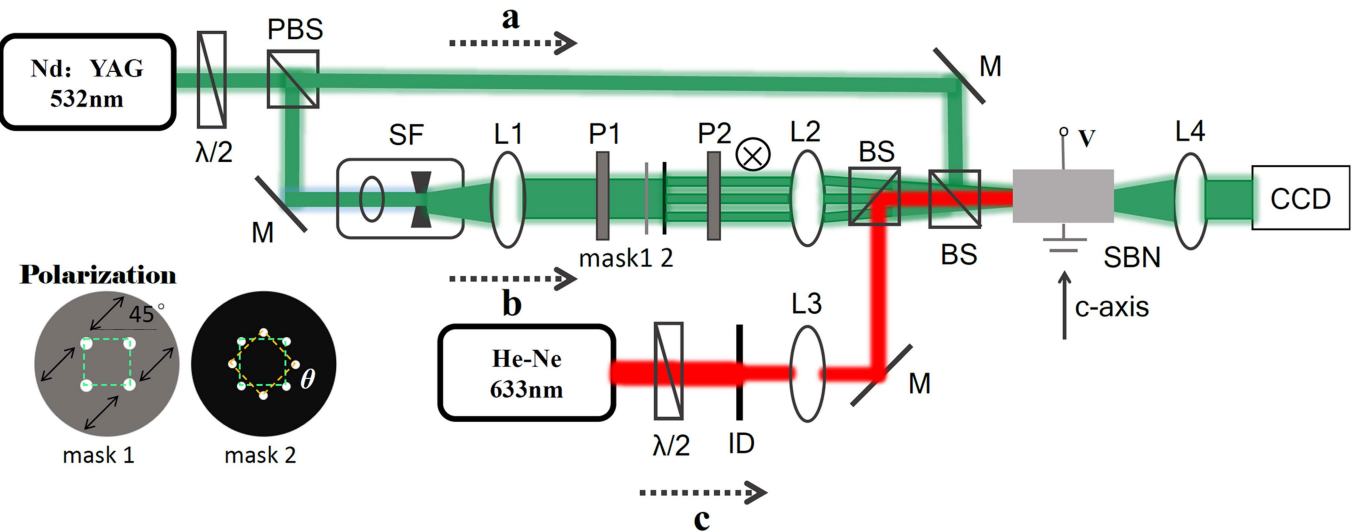
row), $\tan\theta = 3^{-1/2}$ and $p_2 = 1$ (above the LDT point; middle row) and $\tan\theta = 3/4$ and $p_2 = 1$ (bottom row). The two top rows correspond to the incommensurable Pythagorean lattice shown in Fig. 1b. The third row corresponds to the commensurable lattice shown in Fig. 1c.



Extended Data Fig. 2 | Numerical simulation of light propagation to distances beyond the crystal length. **a, b**, Numerical simulations of the light-beam propagation in the incommensurable moiré lattice for central excitation, corresponding to the top and middle rows of Extended Data Fig. 1, but for larger

distances, exceeding the sample length. **c, d**, Similar numerical results, but for an off-centre excitation position in the moiré lattice. $p_2=0.1$ (**a, c**), $p_2=1.0$ (**b, d**), $\theta=\pi/6$. In all cases, a Gaussian beam exciting a single site of the potential is assumed.

Article



Extended Data Fig. 3 | Experimental setup. $\lambda/2$, half-wave plate; PBS, polarizing beam splitter; SF, spatial filter; L, lens; BS, beam splitter; ID, iris diaphragm; M, mirror; P, polarizer; SBN, strontium barium niobate crystal;

CCD, charged-coupled device. Mask 2 is an amplitude mask used to produce two group of sub-lattices with rotation angle θ , and mask 1 is made of a polarizer film.

Extended Data Table 1 | Characteristics of the moiré lattices used in the experiments

Moiré lattice $I(\mathbf{r})$	Sublattice $V(\mathbf{r})$	Diophantine equation	$\tan \theta$
Pythagorean	$\cos(2x) + \cos(2y)$	$a^2 + b^2 = c^2$	b/a
hexagonal	$\sum_{n=1}^3 \cos [2(x \cos \theta_n + y \sin \theta_n)]$	$a^2 + b^2 + ab = c^2$	$\sqrt{3}b/(2a + b)$

For hexagonal lattices $\theta_1 = 0$, $\theta_2 = 2\pi/3$ and $\theta_3 = 4\pi/3$.